Extreme regimes of femtosecond photoemission from a copper cathode in a dc electron gun

P. L. E. M. Pasmans,[1] D. C. van Vugt,[1] J. P. van Lieshout,[1] G. J. H. Brussaard,[1] and O. J. Luiten[1,2,*]

[1]*Department of Applied Physics, Eindhoven University of Technology,*
P.O. Box 13, 5600 MB Eindhoven, The Netherlands
[2]*Institute of Complex Molecular Systems, Eindhoven University of Technology,*
P.O. Box 13, 5600 MB Eindhoven, The Netherlands

The femtosecond photoemission yield from a copper cathode and the emittance of the created electron beams has been studied in a 12 MeV/m, 100 keV dc electron gun over a wide range of laser fluence, from the linear photoemission regime until the onset of image charge limitations and cathode damaging. The measured photoemission curves can be described well with available theory which includes the Schottky effect, second-order photoemission, and image charge limitation. The second-order photoemission can be explained by thermally assisted one-photon photoemission (1PPE) and by above-threshold two-photon photoemission (2PPE). Measurements with a fresh cathode suggest that the 2PPE process is dominant. The beam emittance has been measured for the entire range of initial surface charge densities as well. The emittance measurements of space-charge dominated beams can be described well by an envelope equation with generalized perveance. The dc gun produces 0.1 pC bunches with 25 nm rms normalized emittance, corresponding to a normalized brightness usually associated with rf photoguns. In this experimental study the limits of femtosecond photoemission from a copper cathode have been explored and analyzed in great detail, resulting in improved understanding of the underlying mechanisms.

I. INTRODUCTION

Photoemission electron sources play an essential role in many experiments aimed at the study of ultrafast structural dynamics [1–5]. After creation through photoemission with femtosecond laser pulses, ultrashort electron bunches can be used for electron diffraction and imaging or to enable x-ray diffraction experiments with a free-electron laser (FEL). With ultrafast electron diffraction (UED), ultrafast electron microscopy (UEM), or ultrafast x-ray diffraction, transformations of atomic structures can be captured with *both* atomic spatial resolution *and* atomic temporal resolution [6–14]. These techniques provide a deeper, fundamental understanding of atomic dynamics in matter ranging from solid-state materials like graphene and superconductors to complex biological structures such as proteins and viruses [10–14].

For x-ray FELs, electron bunches are typically created by photoemission in radio-frequency (rf) photoguns and subsequently accelerated in rf linacs to GeV energies to generate x-rays in an undulator. In a recent development the few-MeV pulsed electron beams produced with rf photoguns are applied for electron diffraction, which is a particularly promising approach for attaining ultrashort electron bunches and for gas-phase samples [15,16]. For most applications of electron diffraction and imaging, however, electron energies are preferred in the range of 30–200 keV because of the relatively high elastic scattering cross-section at these energies, the relatively low radiation damage, and the ability to accelerate with stable static fields in a dc photogun [4].

Both metallic and semiconductor photocathodes can be used [1,2]. Semiconductor cathodes typically have a higher yield, but metallic cathodes are generally more stable, have less stringent vacuum requirements, and exhibit prompt emission of the electrons. The latter is particularly relevant if sub-ps temporal resolution is required in a compact setup.

Photoemission has been used and studied extensively for many decades in the context of both photoelectron spectroscopy and photoemission electron sources [17–26]. Most photoemission studies are performed in the low field regime with spectroscopy or in high rf fields for generation of relativistic beams. The application of femtosecond photoemission in a high-field-strength dc gun for UED is a relatively recent development and the ultimate limits of photoemission for UED still need to be explored in detail. The investigation of the different regimes of photoemission is particularly important for single-shot electron diffraction, which requires the generation of as much charge as possible from an illumination area as small as possible.

*o.j.luiten@tue.nl

Here, we report on photoemission yield and emittance measurements in the 12 MeV/m, 100 keV dc electron gun developed for the UED setup at Eindhoven University of Technology. At the time of the experiments, the copper cathode had been in use for 9 months and was not cleaned prior to the measurements. This represents the typical situation when the electron gun is used for UED experiments. The photoemission yield has been studied over a wide range of laser fluence, ranging from the regime of linear photoemission, where a few electrons per μm^2 are extracted from the photocathode, until the onset of image charge limitations and cathode damaging, where 10^3–10^4 electrons per μm^2 are extracted, comparable to the surface charge densities in rf photoguns. The whole fluence range has been measured in the same setup with a single copper cathode illuminated with femtosecond UV laser pulses with a central wavelength of 267 nm. The acceleration field has been varied between 1.23 MV/m and 12.3 MV/m, corresponding to electron energies of 10 keV to 100 keV. Emittance measurements have been performed using waist scans for initial surface charge densities ranging from 10 to 10^3 electrons per μm^2 and for an acceleration field of 12.3 MV/m in order to study the influence of the charge density on beam quality.

In Sec. II, the theoretical framework is presented to describe the femtosecond photoemission for the complete range of fluences and acceleration fields. This includes the Schottky effect, nonlinear photoemission, and image charge limitation. The model for image charge limited photoemission is compared with particle tracking simulations using the general particle tracer (GPT) code. In Sec. II E the theoretical background of beam emittance and brightness is discussed and how to model the emittance evolution of space-charge-dominated beams. The experimental setup for the photoemission yield and emittance measurements is described in Sec. III and the results are presented and discussed in Sec. IV. We find that both the photoemission yield measurements and the measured evolution of the beam emittance agree very well with theoretical model descriptions. For a proper description of the photoemission process it is essential that the Schottky effect, second-order photoemission, and image charge limitation are included. In particular second-order photoemission turns out to play an important role under all conditions relevant for UED or UEM. Measurements with a fresh cathode suggest that above-threshold two-photon emission (2PPE) is the dominant mechanism. The emittance measurements of space-charge dominated beams can be described very well using an envelope equation with generalized perveance. Without any particular efforts to minimize space-charge effects by optimizing the photoemission beam profile, the dc gun produces 0.1 pC bunches—sufficient for single-shot UED—with 25 nm rms normalized emittance from a 25 μm rms spot size. This corresponds to a normalized brightness usually associated with rf photoguns.

II. ULTRAFAST PHOTOEMISSION THEORY

A. Work function and Schottky effect

Photoemission is determined by the (surface) work function ϕ of a material, which is the minimum energy required to remove an electron at the Fermi level from a solid into vacuum. The reported work function of copper (in zero field) lies in the range $\phi_0 = 4.31$–4.91 eV, depending on the orientation of the lattice planes and on the cleaning of the cathode [27,28]. When an external field is applied, the effective work function ϕ is lowered due to the Schottky effect [29]:

$$\phi = \phi_0 - \sqrt{\frac{e^3 \beta G_a}{4\pi\epsilon_0}} \qquad (1)$$

where G_a is the applied acceleration field, e is the electron charge, ϵ_0 is the vacuum permittivity, and β is the field enhancement factor due to surface roughness ($\beta = 1$ for a perfectly flat cathode). Literature values for β range from 1.5 to 500 [23,26]. The work function is lowered by an amount $\Delta\phi = 0.12$ eV for $G_a = 10$ MV/m and $\beta = 1$.

B. Generalized Fowler-DuBridge theory

We apply the generalized Fowler-DuBridge theory [17–19], which is sufficient for our purposes. More advanced theories have recently been developed, such as [30], but these are not relevant to the bare copper emission surface in our setup. Following the generalized Fowler-DuBridge theory the photoemitted current density J can be written as the sum of the partial current densities J_n given by:

$$J_n(\mathbf{r}, t) = a_n \left[\frac{e}{h\nu}(1-R)I(\mathbf{r}, t) \right]^n A_0 T_e^2 f(x_n) \qquad (2)$$

with

$$f(x_n) = \int_0^\infty \ln\left[1 + \exp(-y + x_n)\right] dy \qquad (3a)$$

$$x_n = \frac{nh\nu - \phi}{k_B T_e} \qquad (3b)$$

where a_n are phenomenological coefficients, h is Planck's constant, $h\nu$ is the incident photon energy, R is the surface reflectivity, I is the incident (laser) irradiance, $A_0 = 1.20173 \times 10^6$ A/m²K² is the Richardson constant, T_e is the electron surface temperature, k_B is Boltzmann's constant, and $f(x_n)$ is the Fowler function [17]. The term $a_n[\ldots]^n$ in Eq. (2) is proportional to the probability per unit time of an electron to absorb n photons and to escape [21]. The term $T_e^2 f(x_n)$ in Eq. (2) takes into

account the number of available electrons at the temperature T_e (based on Fermi-Dirac statistics) to overcome the work function of the metal and describes thermally assisted photoemission. For $n = 0$, the partial current reduces to the Richardson equation for thermionic emission, $J_0 = a_0 A_0 T_e^2 \exp(-\phi/k_B T_e)$, with a_0 a dimensionless constant of order unity [31]. For $n \neq 0$, J_n describes n-photon photoemission with constants a_n which can be assessed experimentally or evaluated by microscopic theories. The ratio between the constants can be estimated roughly using the scaling relation [21]: $a_n/a_{n+1} \sim 10^{15}$–10^{18} A/m^2. In Sec. II C it will be shown that for $h\nu - \phi \gg k_B T_e$ the constant a_1 can be related to the (linear) quantum efficiency according to $QE \simeq a_1 A_0 (h\nu - \phi)^2/2k_B^2$. For copper $a_1 = 5 \times 10^{-18}$ m^2/A, as calculated using literature values from [29].

C. Femtosecond photoemission

For photoemission with sub-picosecond laser pulses, the thermodynamic equilibrium between the electron gas and the metal lattice is disturbed during the entire interaction time with the laser pulse [21,22]. The nonequilibrium regime is commonly described by the two-temperature model, in which the electrons and lattice are described by two separated systems with an electron temperature T_e and a lattice temperature T_l. Equilibration between electrons and lattice is governed by the specific heat capacity of the electrons $C_e = \kappa T_e$ and the electron-phonon coupling parameter g. The typical rate for energy exchange g/κ is in the order of 1 K/fs for most metals, implying a time to equilibrium of the order of 1 ps [22]. During the $\sim$100 fs photoemission process the electron temperature T_e may therefore increase significantly with laser intensity $I(\mathbf{r}, t)$. Inspection of the general expression (2) shows that this implies an increase of the thermionic emission J_0. In addition it will result in thermally assisted nonlinear photoemission J_n with a power dependence on I greater than n, in particular thermally assisted second order photoemission for $n = 1$. Equation (2) can be simplified by using the approximation $f(x) \simeq x^2/2 + \pi^2/6$ for the Fowler function, which holds for $x > 1$. For $n = 1$ we then find:

$$J_1(\mathbf{r}, t) \simeq \frac{a_1 A_0 e}{2h\nu} (1 - R) I(\mathbf{r}, t)$$
$$\times \left[\left(\frac{h\nu - \phi}{k_B} \right)^2 + \frac{\pi^2 T_e(\mathbf{r}, t)^2}{3} \right]. \quad (4)$$

For $h\nu - \phi \gg k_B T_e$, i.e., $x_1 \gg 1$, J_1 becomes independent of T_e, resulting in the simple relation between a_1 and the linear QE mentioned in Sec. II B. Generally, $x_n = nh\nu - \phi \gg k_B T_e$ for $n \geq 2$ so then the Fowler function may be approximated by $f(x) \simeq x^2/2$, resulting in:

$$J_2(\mathbf{r}, t) \simeq \frac{a_2 A_0 e^2}{2(h\nu)^2} [(1 - R) I(\mathbf{r}, t)]^2 \left(\frac{2h\nu - \phi}{k_B} \right)^2. \quad (5)$$

Assuming that equilibration of the electrons with the lattice takes place on time scales much longer than the laser pulse duration and that the laser pulse has a Gaussian temporal intensity profile with rms pulse length τ, the final electron temperature in the photoemission process is given by [22]

$$T_{e,\text{peak}}(\mathbf{r}) = \sqrt{\frac{2\alpha}{\kappa} F_a(\mathbf{r}) + T_i^2} \quad (6)$$

where T_i is the initial temperature, α the optical absorption coefficient, and $F_a(\mathbf{r}) \equiv (1 - R)\sqrt{2\pi}\tau I_0(\mathbf{r})$ is the absorbed fluence with $I_0(\mathbf{r})$ the peak laser intensity as a function of position. For copper $\alpha = 7.9 \times 10^7$ m^{-1} for 267 nm [32,33] and $\kappa = 96.8$ J/m^{3}K^2 [34], which gives $\alpha/\kappa = 8 \times 10^5$ m^{2}K^2/J.

Integration of $J_1(\mathbf{r}, t)$ and $J_2(\mathbf{r}, t)$ over times $t \gg \tau$ and using Eq. (6) now yields the final (surface) charge densities $\sigma_1(\mathbf{r})$ and $\sigma_2(\mathbf{r})$:

$$\sigma_1(\mathbf{r}) \simeq \frac{a_1 A_0 e}{2h\nu} \left(\frac{h\nu - \phi}{k_B} \right)^2 F_a(\mathbf{r})$$
$$+ \frac{a_1 A_0 e \pi^2 \alpha}{6h\nu\kappa} F_a(\mathbf{r})^2, \quad (7)$$

$$\sigma_2(\mathbf{r}) \simeq \frac{a_2 A_0 e^2}{4\tau\sqrt{\pi}(h\nu)^2} \left(\frac{2h\nu - \phi}{k_B} \right)^2 F_a(\mathbf{r})^2. \quad (8)$$

The contribution of T_i has been neglected since generally $k_B T_i \ll h\nu - \phi$. The second-order term for σ_1 appears due to the dependence of T_e^2 on I_0 (or F_a).

Equations (7) and (8) show that there are two different mechanisms which can explain a second order dependence of the photoemission yield on the laser fluence. The first mechanism is called thermally assisted one-photon photoemission (1PPE), expressed by the last term in Eq. (7). The second mechanism is called above-threshold two-photon photoemission (2PPE), expressed by Eq. (8). Above-threshold means that more photons are absorbed than the minimal number required to overcome the work function potential [22]. To estimate the relative contributions, the constants b_1 and b_2 are introduced, defined by: $\sigma(\mathbf{r}) = \sigma_1(\mathbf{r}) + \sigma_2(\mathbf{r}) \equiv b_1 F_a(\mathbf{r}) + b_2 F_a(\mathbf{r})^2$. Using $a_1 \simeq 5 \times 10^{-18}$ m^2/A and $a_2 \simeq 5 \times 10^{-33}$ m^4/A^2 from Sec. II B, with the parameters $\alpha/\kappa = 8 \times 10^5$ m^{2}K^2/J, $h\nu = 4.65$ eV, $\phi = 4.3$ eV, and $\tau = 100$ fs, we find $b_1 = 1.1 \times 10^{-5}$ C/J. Assuming thermally assisted 1PPE is the dominant second-order mechanism it follows that $b_2 = 1.7 \times 10^{-6}$ Cm^2/J^2; if above-threshold 2PPE is dominant then $b_2 = 1.3 \times 10^{-6}$ Cm^2/J^2. Both mechanisms could therefore contribute approximately equally to b_2.
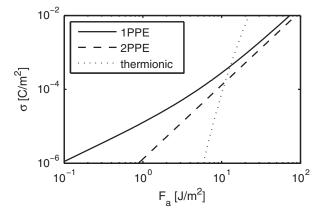
FIG. 1. One-photon photoemission (1PPE) and two-photon photoemission (2PPE) compared with thermionic emission as a function of absorbed fluence.

Obviously, the increase of T_e also enhances the thermionic emission current density J_0, see Eq. (2). In Fig. 1, the surface charge density σ is plotted as a function of the absorbed fluence F_a, for thermionic emission (J_0), single-photon photoemission (J_1), and two-photon photoemission (J_2), calculated using the parameters given above and using $T_i = 300$ K and $a_0 = 1$. To calculate the surface charge density σ from J_0, constant thermionic emission during 1 ps has been assumed. Figure 1 shows that, for these parameters, thermionic emission becomes significant for $F_a > 10$ J/m^2. The curves for 1PPE and 2PPE obtain the same slope for high values of F_a; whether these curves cross depends on the variables $h\nu$, τ, and $\phi(G_a)$, and on the constants a_1, α/κ, and a_2.

D. Image charge limited emission

With increasing laser fluence and, consequently, an increasing photoemitted surface charge density, the photoemission yield eventually becomes suppressed due to image charge. The most elegant way to take the effect of the image charge into account is by including the image charge into the potential barrier for the photoemission process [35]. Here, we apply a simpler model in which we treat the photoemitted electrons as a single sheet which shields the cathode from the acceleration field. The surface charge density threshold σ_{lim} at which the field at the cathode is cancelled is then easily derived analytically [36]: $\sigma_{\text{lim}} \equiv \epsilon_0 \beta G_a$. For $\beta = 1$ and $G_a = 10$ MV/m, $\sigma_{\text{lim}} = 8.9 \times 10^{-5}$ C/m^2.

For the spatial profile of the laser pulse, a cylindrically symmetric Gaussian distribution is assumed with an rms width s. This gives a peak fluence $F_0 \equiv E/2\pi s^2$ for a pulse energy E. The image charge limitation can be included by assuming that the photoemitted surface charge density $\sigma(\mathbf{r})$ is locally limited by σ_{lim}. The fluence F_{lim} is defined as the fluence at which $\sigma(\mathbf{r}) = \sigma_{\text{lim}}$. Integration of $\sigma(\mathbf{r})$ over the Gaussian laser profile gives:

$$\sigma_0 \equiv \frac{Q}{2\pi s^2}$$

$$= \begin{cases} b_1 F_0 + \frac{b_2}{2} F_0^2 & \text{for } F_0 \leq F_{\text{lim}} \\ b_1 F_{\text{lim}} + \frac{b_2}{2} F_{\text{lim}}^2 + \sigma_{\text{lim}} \ln\left(\frac{F_0}{F_{\text{lim}}}\right) & \text{for } F_0 \geq F_{\text{lim}}. \end{cases}$$

$$(9)$$

Note that for $F_0 \leq F_{\text{lim}}$, σ_0 is the peak surface charge density; for $F_0 \geq F_{\text{lim}}$, σ_0 ($\neq \sigma_{\text{lim}}$) becomes an "effective" peak surface charge density. Using b_1 and b_2 for 1PPE from the previous section gives $F_{\text{lim}} = 4.7$ J/m^2 for $\beta = 1$ and $G_a = 10$ MV/m. Note that $F_{\text{lim}} < 10$ J/m^2 for the chosen parameters, so that thermionic emission can safely be neglected below the onset of image charge limited emission.

In Fig. 2, Eq. (9) is compared with particle tracking simulations to check the validity of the model, using the general particle tracer (GPT) code [37]. The model is based on a homogeneous sheet of electrons, while the simulations are performed with electrons distributed according to a randomized Gaussian distribution in three dimensions. For these simulations, we created an electron distribution with 10^6 macroparticles, with a temporal width of $\tau = 100$ fs, and with a beam temperature of $k_B T_b = 0.5$ eV. Spatially, the cylindrically symmetric distribution is split in a part for first-order photoemission with a spatial width $s_1 = 30$ μm and first-order coefficient $b_1 = 1 \times 10^{-5}$ C/J, and in a part for second-order photoemission with a spatial width $s_2 = s_1/\sqrt{2}$ and second-order coefficient $b_2 = 2 \times 10^{-6}$ Cm^2/J^2. The parameters b_1 and b_2 also determine the amount of initially created electron charge. The electron distribution is created at $z = 0.1$ nm in a global acceleration field $G_a = 10$ MV/m which accelerates the electrons in the positive z direction. Space charge and image charge effects are taken into account. Electrons which cross the xy-plane at $z = 0$ are removed and electrons which cross the xy-plane at $z = 1$ mm are
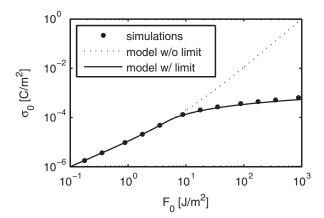

FIG. 2. Peak surface charge density versus peak laser fluence, simulated using GPT.

counted as electrons that are photoemitted. Figure 2 shows that the model and simulations give the same result.

E. Emittance and brightness

The photoemission process influences the beam quality of the emitted electron bunches as expressed by emittance and brightness. Emittance is a measure for the focusability of a beam and is proportional to the area of the 2D projection of a bunch on (x, p_x) phase space. The normalized (rms) emittance is defined as:

$$\epsilon_{n,x} = \frac{1}{mc} \sqrt{\langle x^2 \rangle \langle p_x^2 \rangle - \langle x p_x \rangle^2} \tag{10}$$

where m is the electron mass, c is the speed of light, and $\langle \rangle$ indicates averaging over the electron distribution in the bunch. The emittances $\epsilon_{n,y}$ and $\epsilon_{n,z}$ are defined analogously. Geometrical emittance ϵ_x is proportional to the area in trace space (x, x') and is related to the normalized emittance according to $\epsilon_{n,x} \equiv \gamma \beta_f \epsilon_x$ (where γ is the Lorentz factor and β_f the bunch speed normalized to the speed of light). In the fields of accelerator physics and electron microscopy, brightness is commonly used as a measure for beam quality and includes the bunch charge Q as well. The normalized transverse brightness B_n is defined as [38]:

$$B_n \equiv \frac{1}{mc} \frac{Q}{(2\pi)^2 \epsilon_{n,x}^2}. \tag{11}$$

The initial, or thermal, emittance is given by:

$$\epsilon_{n,T} = s \sqrt{\frac{k_B T_b}{mc^2}} \tag{12}$$

where s is the rms laser spot size on the cathode and T_b the effective source temperature. The source temperature is related to the difference between the photon energy and effective work function: $k_B T_b \simeq (h\nu - \phi)/3$ [29]. For $h\nu = 4.65$ eV, $G_a = 10$ MV/m, $\beta = 1$, and $\phi_0 = 4.31$ eV, we have $k_B T_b \simeq 0.15$ eV. Due to surface roughness, adsorbed compounds, the spectral width of (femtosecond) laser pulses, and other deviations from ideal photoemission, the beam temperature is higher in practice. The experimental thermal emittance is typically a factor 2-3 higher than the theoretical value [29]. In our calculations and simulations we assume $k_B T_b = 0.5$ eV.

The transverse emittance can be measured through a waist scan. The principle of a waist scan is to measure the rms electron beam size s_x as a function of lens strength at a fixed position after the (electron-optical) lens. In the approximation that the bunch length is much larger than the bunch diameter, the propagation including space charge can be described to a reasonable approximation with the following single differential equation for the beam envelope [39]:

$$s_x'' - \frac{\epsilon_x^2}{s_x^3} - \frac{K}{s_x} = 0 \tag{13}$$

where space charge is included by the term $-K/s_x$. Here K is the generalized perveance which is proportional to the beam current. For a continuous 100 keV electron beam with a top-hat profile and current I_b, the generalized perveance is given by $K = I_b/I_P$ with $I_P \simeq 2.4 \times 10^3$ A [39].

III. EXPERIMENTAL SETUP

The experiments have been performed in the UED setup at Eindhoven University of Technology as described in [3,40–42].

A. Laser fluence

To generate ultrashort laser pulses, a Ti:sapphire oscillator (Coherent, Mantis) and a Ti:sapphire regenerative amplifier (Coherent, Legend Elite) are used. The amplified laser pulses have a central wavelength of 800 nm ($h\nu = 1.55$ eV) with a typical bandwidth of 32 nm (FWHM) and with a typical pulse length of 60 fs (FWHM). UV light pulses with a central wavelength of 267 nm ($h\nu = 4.65$ eV) are generated through third harmonic generation (THG) using thin BBO crystals. With a $\lambda/2$-waveplate in a motorized rotation mount before the THG crystals, the energy of the UV pulses can be varied between 0.1 μJ and 4 μJ. The UV pulses are focused onto the cathode in the electron gun, using a lens with a focal length of $f = 1$ m. By changing the distance between this lens and the cathode or by removing the lens, the spot size s on the cathode can be varied (see Table I). The spot size s and energy per pulse E are measured using a beam splitter between the lens and the cathode. The spot size s is determined using a UV camera at the same distance behind the lens as the cathode. The camera image is subsequently fitted with a two-dimensional cylindrically symmetric Gaussian profile. The energy per pulse E is determined with a UV diode (EPIGAP, EPD-440-0/1.45) which has been calibrated using a power meter (Coherent, LabMax Top with J-10MT-10kHz sensor). The signal of the UV diode is recorded with a digital oscilloscope (Agilent, DSO7054A). To calculate the absorbed energy E_a, the (measured) 85% transmission of the vacuum window (between lens and cathode) and the (theoretical) 34% reflectivity of the copper cathode are taken into account [32,33]. The

TABLE I. UV spot size for different lens positions with $f = 1$ m.

Lens position	$s [\mu$m]
No lens	503.5 ± 2.8
Lens @ 0.800 m	168.7 ± 1.4
Lens @ 0.950 m	39.9 ± 0.1
Lens @ 0.975 m	32.8 ± 0.7

absorbed peak fluence is given by $F_0 = E_a/2\pi s^2$. The angle of incidence of the UV pulses onto the cathode is $\approx 3°$ with respect to normal incidence, so polarization effects are negligible.

B. Charge density

The photocathode material is high-purity (99.99%), oxygen-free copper (Outokumpu, ASTM C10100), which was machined using single-diamond turning. The measurements have been performed with a cathode that had been in use for 9 months, except for a single measurement curve, which has been measured with a fresh cathode (as will be discussed in Sec. IV E). The cathode has a flat circular area in the center with a diameter of 1 mm. The grooves from the diamond turning are used for alignment of the UV pulses onto the center of the cathode. The center of the grounded anode is at 11.4 mm from the cathode and has a circular opening with a 8.0 mm radius [41]. A maximal voltage difference of 100 kV can be applied, which corresponds to an acceleration field of -12.3 MV/m at the cathode, as calculated with the Poisson solver SUPERFISH. During the photoemission yield measurements, the voltage was varied from -100 kV to -10 kV in steps of 10 kV.

A magnetic coil is positioned after the photogun to focus the photoemitted electrons onto a Faraday cup. The current through the coil is optimized for each acceleration voltage to collect the maximal amount of charge. The Faraday cup has an opening diameter of 32 mm with a rather long core of 96 mm, to prevent secondary electrons from escaping [43]. The Faraday cup is connected to a charge amplifier (Canberra, 2004) which is connected to the digital oscilloscope (Agilent, DSO7054A). The scope trace is used to determine the collected charge Q. The combination of Q and the spot size s from the UV camera is used to calculate the (effective) peak charge density $\sigma_0 = Q/2\pi s^2$.

C. Data aquisition

The digital oscilloscope is connected to a computer which reads out the peak value of the trace from the UV diode and the complete trace from the charge amplifier. The trace from the charge amplifier has been fitted with an exponentially decaying step function in Matlab. The photoemission yield measurements have been performed for 10 voltages, 4 lens positions, and 360 steps of $\sim 1°$ for the rotation mount (to vary the intensity). With 5 acquisitions per settings, this gives a total number of 72 000 data points. The actual number of data points is somewhat less, since data points with $Q > 12$ pC (clipping in charge amplifier) and with $E < 100$ nJ (noise level) have been discarded.

D. Waist scans

Waist scans to determine transverse bunch emittance have been performed using two magnetic coils. A first coil (as used for charge collection onto a Faraday cup) at 58 mm

and a second coil at 320 mm behind the cathode. The first coil has an inner radius of 30.0 mm, an outer radius of 51.0 mm, a length 51.7 mm and 1055 windings. The second coil has an inner radius of 30.0 mm, an outer radius of 45.9 mm, a length 38.3 mm and 859 windings. The second coil is used to change the focusing strength, with the first condenser lens at a constant current of $I_{C1} = 2.91$ A. The electron bunches are recorded as function of the current I_{C2} through the second coil on a detector at a distance of 1.7 m from the cathode. The detector consists of a microchannel plate with a phospor screen (Burle Industries, APD 6040FM 12/10/8 I 60:1 P20) and a monochrome 10.7 megapixel camera (Lumenera, Lw11057M1). The bunches have been created from a laser spot on the cathode with an rms size $s = 25.0 \pm 0.2$ μm. For more details on the experimental setup, see Ref. [42].

IV. RESULTS AND DISCUSSION

A. Photoemission yield

In Fig. 3 measurements are presented of the peak surface charge density $\sigma_0 \equiv Q/(2\pi s^2)$ (see Sec. II D) as a function of peak fluence F_0 for acceleration voltages of 10 and 100 kV. Each dot is an average of grouped data points (for logarithmic distributed bins) with error bars given by ± 1 standard deviation (systematic errors have not been included). The measured data points for the different lens positions have been combined into a single data set by plotting σ_0 versus F_0 instead of Q versus E. The data points for the different lens positions connect very well, although some small shifts are noticeable. By moving the lens, the alignment on the cathode might have changed slightly, which might influence the photoemission yield due to
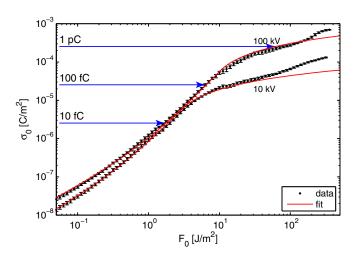
FIG. 3.   Measured peak surface charge density $\sigma_0 \equiv Q/(2\pi s^2)$ as a function of peak fluence F_0 for acceleration voltages of 10 and 100 kV, corresponding to acceleration fields (G_a) of 1.23 and 12.3 MV/m. The blue arrows indicate the conditions at which waist scans have been performed (at 100 kV).

variations in the laser beam profile or due to local variations like surface roughness or quantum efficiency [26].

The damage threshold of copper is on the order of $1 \, \text{PW/m}^2$ for sub-ps pulses [22]. This is equivalent to a fluence on the order of $100 \, \text{J/m}^2$ for a pulse length of 100 fs. From this fluence an increase in slope is visible in Fig. 3, which thus seems to be an indication of cathode damaging.

The data have been fitted up to $F_0 = 50 \, \text{J/m}^2$ using Eq. (9) for each acceleration voltage, with fitting parameters b_1 and b_2, and the assumption $\beta = 1$ to calculate F_{lim} from b_1 and b_2. The fitted curves for 10 and 100 kV are shown in Fig. 3 and demonstrate that the measured data agree well with the theory. Similar curves have been recorded and fitted equally well with theory for acceleration voltages 20,30,...,80,90 kV. For 100 kV acceleration voltage, corresponding to $G_a = 12.3 \, \text{MV/m}$, we find $b_1 = 5.4 \times 10^{-7} \, \text{C/J}$ and $b_2 = 5.4 \times 10^{-7} \, \text{Cm}^2/\text{J}^2$. This means that at a peak fluence $F_0 = 0.1 \, \text{J/m}^2$ 80% of the electron yield is due to a linear photoemission process, while at $F_0 = 10 \, \text{J/m}^2$ 95% of the electron yield can be attributed to second order photoemission. The fitted parameters b_1 and b_2 and their dependence on acceleration field are discussed in more detail in the following two sections.

B. Schottky effect

The fitted parameter b_1 is shown in Fig. 4 as a function of the acceleration field G_a. The error bars are based on 95% confidence bounds for the fit and do not include systematic errors. The relatively large error margins are a result of the correlation with b_2 (see Eq. (9)) and therefore indicate the range of possible values of b_1. An increase of b_1 as a function of G_a is observed due to the Schottky effect. The data have been fitted using the first-order coefficient of Eq. (7) with the work function ϕ from Eq. (1), assuming $h\nu = 4.65 \, \text{eV}$ and $\beta = 1$. The values obtained from the fit (with confidence bounds from the fit only) are $\phi_0 = 4.48 \pm 0.01 \, \text{eV}$ for the zero field work
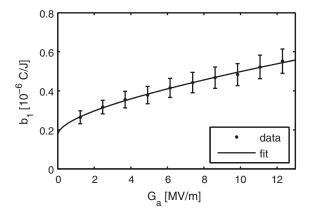
function and $a_1 = (3.4 \pm 0.4) \times 10^{-19} \, \text{m}^2/\text{A}$. The value for ϕ_0 fits well within the range $\phi_0 = 4.31\text{--}4.91 \, \text{eV}$ found in literature [27,28]. The value for a_1 is more than an order of magnitude below the value of $5 \times 10^{-18} \, \text{m}^2/\text{A}$ for atomically clean copper derived from [29] (see Sec. II B). Surface contamination could explain the lower value, especially in view of the fact that the cathode has been in use for 9 months (see also Sec. IV E) and was not cleaned prior to the measurement; the only form of cleaning is the illumination with the UV light pulses.

C. Second-order photoemission

The fitted parameter b_2 is shown in Fig. 5 as a function of the acceleration field G_a. The error bars are based on 95% confidence bounds for the fit and do not include systematic errors. The second-order coefficient b_2 can be explained by thermally assisted one-photon photoemission (1PPE) or by above-threshold two-photon photoemission (2PPE). The case of 1PPE can be described with the second-order coefficient of Eq. (7), which does not depend on G_a. With a_1 from the previous section, the mean value of b_2 gives $\alpha/\kappa = (7.2 \pm 0.2) \times 10^6 \, \text{m}^2\text{K}^2/\text{J}$, which is an order of magnitude larger than the value $\alpha/\kappa = 8 \times 10^5 \, \text{m}^2\text{K}^2/\text{J}$ obtained from literature (see Sec. II C). The case of 2PPE can be described using Eq. (8), with the same parameters as in the previous section combined with the fitted value for ϕ_0. Assuming $\tau = 100 \, \text{fs}$, a_2 has been used as a fit parameter. The fitted value $a_2 = (4.1 \pm 0.2) \times 10^{-33} \, \text{m}^4/\text{A}^2$, which agrees well with the value of $a_2 \approx 5 \times 10^{-33} \, \text{m}^4/\text{A}^2$ as estimated in Sec. II C. It is not possible to determine from the experimental data whether the 1PPE or the 2PPE mechanism determines the second-order slope. However, in case of 2PPE, the fitted value b_2 can be explained well with a value for a_2 which is in line with literature values, whereas in case of 1PPE the fitted value would have to be explained with a value for α/κ which is $\sim 10\times$ larger than literature values. This could be an indication that 2PPE is the dominant process causing the

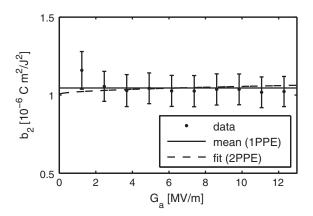FIG. 4.   First-order coefficient b_1 as a function of acceleration field G_a.

FIG. 5.   Second-order coefficient b_2 as a function of acceleration field G_a.

second order photoemission. This is supported by additional measurements on a new cathode, which will be presented in Sec. IV E.

D. Image charge limited emission

The image charge limited emission becomes apparent in Fig. 3 at a fluence $F_a \approx 10$ J/m^2. The influence of the acceleration field is also clear. The data agree well with the model from Sec. II D for $\beta = 1$. For 100 kV, the fitted curve in Fig. 3 is slightly above the measured data points. This small discrepancy would increase with increasing β. The measurements thus indicate that β should be of order unity, which agrees well with $\beta = 1.5 \pm 0.2$ for an rf photogun reported in Ref. [23], and is in disagreement with values up to 500 reported in Ref. [26].

E. New cathode

The cathode from which the above results were obtained, had been in use for 9 months at the time of the measurements. After replacing the cathode and training of the dc gun, a single yield measurement has been performed with the new cathode for an acceleration voltage of 100 kV and a spot size $s = 90.3 \pm 0.5$ μm. For this measurement another Faraday cup has been used which was mounted in the sample chamber of the UED setup. The Faraday cup consists of a 20×20 mm^2 block of copper with a thickness of 8 mm. Due to the back scattered fraction of the electrons at 100 keV, the charge measured with this Faraday cup may be somewhat lower, maximally 30%, than if the same had been used as described in Sec. III B. The charge amplifier and the UV diode are identical. The result of this measurement is shown in Fig. 6, along with the measurement at 100 kV for the other cathode. The data has been fitted using Eq. (9) with the assumption $\beta = 1$. Note that it is also
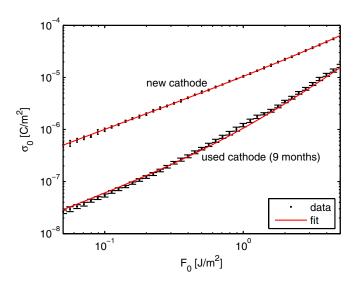
TABLE II. Photoemission coefficients for the new and used cathodes.

	b_1[C/J]	b_2[Cm^2/J^2]
new cathode	$(1.00 \pm 0.01) \times 10^{-5}$	$(1.13 \pm 0.07) \times 10^{-6}$
used cathode	$(5.5 \pm 0.5) \times 10^{-7}$	$(1.02 \pm 0.07) \times 10^{-6}$

assumed that the reflectivity of the cathode has remained constant. The fitted coefficients are shown in Table II (with 95% confidence bounds from the fit).

The value of b_1 for the new cathode agrees very well with the estimated $b_1 = 1.1 \times 10^{-5}$ C/J from Sec. II C. Apparently, the aging effect of the cathode is quite significant, which is also known from literature [25]. Interestingly, the value of b_2 is almost similar for the new and used cathode. This implies that the electron yield of the new cathode is almost entirely due to a linear photoemission process over the entire range of fluences shown in Fig. 6, in contrast to the used cathode. The fact that the measured charge may have been slightly underestimated due to the use of a Faraday cup with a simpler construction does not change these conclusions. In the case of 1PPE this would imply that $a_1 \alpha / \kappa$ is constant for both cathodes and in the case of 2PPE that a_2 is constant. For constant a_1, the increase of b_1 could only be explained by assuming that the work function has decreased to a value $\phi_0 = 3.49$ eV for the new cathode, which is far below literature values and therefore not very likely. A better explanation is that a_1 has increased to a value of 6×10^{-18} m^2/A for the new cathode, in good agreement with the value of 5×10^{-18} m^2/A for atomically clean copper derived from [29]. In the case of 1PPE, however, the increase of a_1 should also result in an increase of b_2 with constant α / κ for both cathodes. The fact that the value of b_2 remains the same is therefore an indication that the second-order photoemission is mainly the result of 2PPE.

F. Emittance and brightness

Figure 7 shows waist scans performed for 100 keV electron bunches with bunch charges of 10 fC, 100 fC, and 1 pC created from a laser spot on the cathode with an rms size $s = 25$ μm. The conditions at which these waist scans have been performed are also indicated by the arrows in Fig. 3. Each data point in Fig. 7 has been obtained from five bunches imaged onto the detector (with one image per bunch). Examples of these images are shown in Fig. 8. For each image the background is subtracted and the beam center is determined from integrated intensity profiles, along both the horizontal and vertical direction, which are fitted with a Gaussian function. The pixel intensity is plotted as a function of the distance to the beam center and fitted with a Gaussian function, which provides the rms beam width. The analysis assumes a cylindrically symmetric Gaussian electron distribution. This assumption
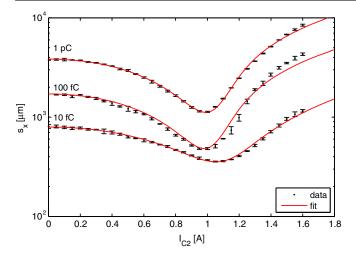

FIG. 6. Measured photoemitted yield at an acceleration voltage of 100 kV for the new and used cathodes.

FIG. 7.   Waist scans for different bunch charges.

TABLE III.   Fitted beam parameters.

Q	ϵ_x [nm]	s_0 [μm]	z_o [m]	K [$-$]
10 fC	(39 ± 2)	(159 ± 2)	(-0.67 ± 0.05)	$(8.1 \pm 0.6) \times 10^{-8}$
100 fC	(41 ± 3)	(145 ± 12)	(-2.63 ± 0.25)	$(5.1 \pm 0.2) \times 10^{-7}$
1 pC	(198 ± 15)	(303 ± 18)	(-2.52 ± 0.09)	$(1.9 \pm 0.1) \times 10^{-6}$

parameters, with 95% confidence bounds from the fitting routine, are listed in Table III.

The initial beam parameters are compared with theoretical parameters for 0 fC (i.e., without space charge) calculated with parameters obtained from particle tracking simulations with GPT [37]. The GPT simulations are performed for the gun and the first magnetic coil using 10000 macroparticles with space charge included using the mesh-based 3D space routine in GPT (except for 0 fC, where no space charge is included). For both the calculations and the simulations, a Gaussian beam at the cathode with $k_B T_b = 0.5$ eV, $s = 25$ μm, and $\tau = 100$ fs is assumed. The parameters ϵ_x, s_0, and z_o are determined at the position of the second condenser lens and are presented in Table IV. The slight difference in the parameters s_0 and z_0 between the theoretical and simulated parameters for 0 fC can be attributed to the fact that the field from the first magnetic coil is not negligible inside the gun, which is assumed for the theoretical beam model. The difference between the parameters obtained with and without Coulomb interactions clearly shows the effect of space charge on emittance and beam divergence.

Comparing Tables III with IV, the parameters are in very good agreement for 10 fC. For 100 fC and 1 pC, the model and the GPT simulations start to deviate; it is interesting to note that the fitted emittances are actually lower than the

is valid for 10 fC bunches, but for 100 fC and especially for 1 pC bunches the distribution becomes less Gaussian, less symmetric, and less smooth, as is visible in Fig. 8. Although the distribution becomes distorted due to space-charge effects and image charge forces during photoemission, the analysis method nevertheless provides a reasonable rms beam width.

Equation (13) is used to describe the space-charge dominated beam propagation with the generalized perveance K as a fit parameter. A Gaussian beam is assumed described by a transverse geometrical emittance ϵ_x and a virtual source size s_0 at position z_o, which are all used as fit parameters. Details on the modeling of the magnetic lens strength as a function of current I_{C2} can be found in Ref. [42]. The fitted curves are shown in Fig. 7. The fitted
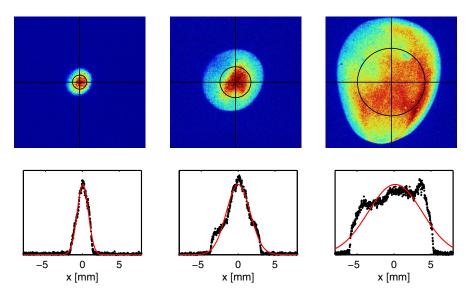

FIG. 8.   Top row: images of electron bunches for $I_{C2} = 0.1$ A for 10 fC, 100 fC, and 1 pC (from left to right); the black lines indicate the fitted beam center and rms beam width. Bottom row: horizontal lineouts (black curves) averaged over 40 pixels in the vertical direction; the lineouts are fitted with Gaussian functions shown by the red curves.

TABLE IV. Beam parameters from theory/GPT.

Q	ϵ_x [nm]	s_0 [μm]	z_o [m]	τ [ps]	K [−]
0 fC (theory)	37.7	194	0.542	0.13	
0 fC (GPT)	37.7	203	0.412	0.14	
10 fC	40.5	168	−0.806	8	1×10^{-7}
100 fC	70.7	130	−1.032	19	6×10^{-7}
1 pC	285	273	−1.312	29	4×10^{-6}

emittances obtained from GPT simulations. One possible explanation is that the nonlinear photoemission process, which is not included in the GPT simulations, may give rise to a lower emittance. Moreover, the real beam profiles, as shown in Fig. 7, are somewhat asymmetric, especially for 1 pC, which will influence the space-charge dynamics during propagation. A detailed analysis of the waist scan data with GPT would require using initial simulation conditions based on the measured laser beam profile, in combination with a model for the nonlinear photoemission process. This is outside the scope of this paper. It is instructive, however, to make estimates for the perveance K using GPT and see whether the K values obtained from the fits make sense. Table IV gives the values of the bunch length τ at the detector from the GPT simulations and the values of K using $I_b \simeq Q/4\tau$ ($\approx$63% of the peak current) as an estimate for the current. We find that the order of magnitude of the estimated values for $K = I_b/I_P$ is in agreement with the fitted values.

The 100 fC bunches with a normalized emittance of 25 nm rad obtained from the waist scans analysis, have the same transverse normalized brightness [Eq. (11)] as 160 pC bunches with a normalized emittance of 1 μm rad, which corresponds to a brightness usually associated with rf photoguns. By optimizing the laser beam profile space-charge effects may be reduced, which would result in an even higher brightness.

V. CONCLUSIONS AND OUTLOOK

Photoemission yield and emittance measurements have been reported for the dc electron gun of the UED setup at Eindhoven University of Technology. The photoemission yield has been studied over a wide range of laser fluence, from the linear photoemission regime until the onset of image charge limitations and cathode damaging. The measured curves can be explained well with available theory including the Schottky effect, second-order photoemission, and image charge limitation. A low field enhancement factor of $\beta = 1$ works best to fit the data. The second-order photoemission can be explained by thermally assisted one-photon emission (1PPE) and by above-threshold two-photon emission (2PPE). At the time of the experiments, the copper cathode had been in use for 9 months and was not cleaned prior to the measurements. Additional measurements with a fresh cathode suggest that

the 2PPE process is dominant. Two photons would make the highly occupied Cu d-band accessible for photoemission, which could explain the quite high efficiency of this process. The measurements with the new cathode are also an indication of cathode degradation in time. This stresses the importance of measuring the photoemission yield on a day-to-day basis (if bunch charge is an important parameter) and of regularly cleaning or replacing the cathode (if yield is important).

The influence of the initial charge density on the beam emittance has been studied. The emittance measurements of space-charge dominated beams are described well by an envelope equation with generalized perveance. We find that the transverse brightness obtained with a 12 MV/m, 100 keV dc photogun is comparable to the brightness of rf photoguns.

We have explored the limits of femtosecond photoemission in a dc gun and understand the underlying mechanisms. It is found that for applications such as UED and UEM, the femtosecond photoemission process will be nonlinear under most relevant conditions. To investigate to what extent the beam quality could further be improved, the second order photoemission process and its dependence on the band structure of the cathode material should therefore be studied in greater detail. This could, for example, be achieved through variation of the laser wavelength, pulse length, and profile, in combination with additional measurements of the electron bunch length and energy spread.

[1] T. Rao and D. H. Dowell, *An Engineering Guide to Photoinjectors* (CreateSpace, 2013).

[2] F. Stephan and M. Krasilnikov, in *Synchrotron Light Sources and Free-Electron Lasers* (Springer, New York, 2016), p. 561.

[3] T. van Oudheusden, E. F. de Jong, S. B. van der Geer, W. P. E. M. Op 't Root, and O. J. Luiten, Electron source concept for single-shot sub-100 fs electron diffraction in the 100 keV range, J. Appl. Phys. **102**, 093501 (2007).

[4] F. Carbone, P. Musumeci, O. J. Luiten, and C. Hebert, A perspective on novel sources of ultrashort electron and X-ray pulses, Chem. Phys. **392**, 1 (2012).

[5] F. O. Kirchner, S. Lahme, F. Krausz, and P. Baum, Coherence of femtosecond single electrons exceeds biomolecular dimensions, New J. Phys. **15**, 063021 (2013).

[6] A. H. Zewail and J. M. Thomas, *4D Electron Microscopy* (Imperial College Press, London, 2010).

[7] R. M. van der Veen, O.-H. Kwon, A. Tissot, A. Hauser, and A. H. Zewail, Single-nanoparticle phase transitions visualized by four-dimensional electron microscopy, Nat. Chem. **5,** 395 (2013).

[8] M. Gao, C. Lu, H. Jean-Ruel, L. C. Liu, A. Marx, K. Onda, S. Koshihara, Y. Nakano, X. Shao, T. Hiramatsu, G. Saito, H. Yamochi, R. R. Cooney, G. Moriena, G. Sciaini, and R. J. D. Miller, Mapping molecular motions leading to charge delocalization with ultrabright electrons, Nature (London) **496,** 343 (2013).

[9] M. Hada, K. Pichugin, and G. Sciaini, Ultrafast structural dynamics with table top femtosecond hard X-ray and electron diffraction setups, Eur. Phys. J. Spec. Top. **222,** 1093 (2013).

[10] S. Schäfer, W. Liang, and A. H. Zewail, Primary structural dynamics in graphite, New J. Phys. **13,** 063030 (2011).

[11] N. Erasmus, M. Eichberger, K. Haupt, I. Boshoff, G. Kassier, R. Birmurske, H. Berger, J. Demsar, and H. Schwoerer, Ultrafast Dynamics of Charge Density Waves in $4H_b$-TaSe$_2$ Probed by Femtosecond Electron Diffraction, Phys. Rev. Lett. **109,** 167402 (2012).

[12] E. Blackburn, J. Chang, M. Hücker, A. T. Holmes, N. B. Christensen, R. Liang, D. A. Bonn, W. N. Hardy, U. Rütt, O. Gutowski, M. v. Zimmermann, E. M. Forgan, and S. M. Hayden, X-Ray Diffraction Observations of a Charge-Density-Wave Order in Superconducting Ortho-II YBa$_2$Cu$_3$O$_{6.54}$ Single Crystals in Zero Magnetic Field, Phys. Rev. Lett. **110,** 137004 (2013).

[13] L. Redecke *et al.*, Natively inhibited Trypanosoma brucei Cathepsin B structure determined by using an X-ray laser, Science **339,** 227 (2013).

[14] M. M. Seibert *et al.*, Single mimivirus particles intercepted and imaged with an X-ray laser, Nature (London) **470,** 78 (2011).

[15] S. P. Weathersby *et al.*, Mega-electron-volt ultrafast electron diffraction at SLAC National Accelerator Laboratory, Rev. Sci. Instrum. **86,** 073702 (2015).

[16] X. H. Lu, C. X. Tang, R. K. Li, H. To, G. Andonian, and P. Musumeci, Generation and measurement of velocity bunched ultrashort bunch of pC charge, Phys. Rev. ST Accel. Beams **18,** 032802 (2015).

[17] R. H. Fowler, The analysis of photoelectric sensitivity curves for clean metals at various temperatures, Phys. Rev. **38,** 45 (1931).

[18] L. A. DuBridge, Theory of the energy distribution of photoelectrons, Phys. Rev. **43,** 727 (1933).

[19] J. H. Bechtel, W. Lee Smith, and N. Bloembergen, Two-photon photoemission from metals induced by picosecond laser pulses, Phys. Rev. B **15,** 4557 (1977).

[20] *Photoemission and the Electronic Properties of Surfaces*, edited by B. Feuerbacher, B. Fitton, and R. F. Willis (John Wiley & Sons, New York, 1978).

[21] M. Peloi, G. Ferrini, G. Banfi, G. Secondi, and F. Parmigiani, Non-linear photoemission from polycrystalline molybdenum irradiated by 790 nm–150 fs laser pulses, Solid State Commun. **118,** 339 (2001).

[22] G. Ferrini, F. Banfi, C. Giannetti, and F. Parmigiani, Non-linear electron photoemission from metals with ultrashort pulses, Nucl. Instrum. Methods Phys. Res., Sect. A **601,** 123 (2009).

[23] P. Musumeci, L. Cultrera, M. Ferrario, D. Filippetto, G. Gatti, M. S. Gutierrez, J. T. Moody, N. Moore, J. B. Rosenzweig, C. M. Scoby, G. Travish, and C. Vicario, Multiphoton Photoemission from a Copper Cathode Illuminated by Ultrashort Laser Pulses in an rf Photoinjector, Phys. Rev. Lett. **104,** 084801 (2010).

[24] Z. Tao, H. Zhang, P. M. Duxbury, M. Berz, and C.-Y. Ruan, Space charge effects in ultrafast electron diffraction and imaging, J. Appl. Phys. **111,** 044316 (2012).

[25] F. Zhou, A. Brachmann, F.-J. Decker, P. Emma, S. Gilevich, R. Iverson, P. Stefan, and J. Turner, High-brightness electron beam evolution following laser-based cleaning of a photocathode, Phys. Rev. ST Accel. Beams **15,** 090703 (2012).

[26] H. Chen, Y. Du, W. Gai, A. Grudiev, J. Hua, W. Huang, J. G. Power, E. E. Wisniewski, W. Wuensch, C. Tang, L. Yan, and Y. You, Surface-Emission Studies in a High-Field RF Gun based on Measurements of Field Emission and Schottky-Enabled Photoemission, Phys. Rev. Lett. **109,** 204802 (2012).

[27] P. O. Gartland, S. Berge, and B. J. Slagsvold, Photoelectric Work Function of a Copper Single Crystal for the (100), (110), (111), and (112) Faces, Phys. Rev. Lett. **28,** 738 (1972).

[28] D. H. Dowell, F. K. King, R. E. Kirby, J. F. Schmerge, and J. M. Smedley, *In situ* cleaning of metal cathodes using a hydrogen ion beam, Phys. Rev. ST Accel. Beams **9,** 063502 (2006).

[29] D. H. Dowell and J. F. Schmerge, Quantum efficiency and thermal emittance of metal photocathodes, Phys. Rev. ST Accel. Beams **12,** 074201 (2009).

[30] K. L. Jensen, N. A. Moody, D. W. Feldman, E. J. Montgomery, and P. G. OShea, Photoemission from metals and cesiated surfaces, J. Appl. Phys. **102,** 074902 (2007).

[31] C. R. Crowell, The Richardson constant for thermionic emission in Schottky barrier diodes, Solid State Electron. **8,** 395 (1965).

[32] Refractive index database, http://refractiveindex.info.

[33] P. B. Johnson and R. W. Christy, Optical constants of the noble metals, Phys. Rev. B **6,** 4370 (1972).

[34] Z. Lin, L. V. Zhigilei, and V. Celli, Electron-phonon coupling and electron heat capacity of metals under conditions of strong electron-phonon nonequilibrium, Phys. Rev. B **77,** 075133 (2008).

[35] D. M. Riffe, X. Y. Wang, M. C. Downer, D. L. Fisher, T. Tajima, and J. L. Erskine, Femtosecond thermionic emission from metals in the space-charge-limited regime, J. Opt. Soc. Am. B **10,** 1424 (1993).

[36] A. Valfells, D. W. Feldman, M. Virgo, P. G. O'Shea, and Y. Y. Lau, Effects of pulse-length and emitter area on virtual cathode formation in electron guns, Phys. Plasmas **9,** 2377 (2002).

[37] The general particle tracer (gpt) code, http://www.pulsar.nl.

[38] O. J. Luiten, B. J. Claessens, S. B. van der Geer, M. P. Reijnders, G. Taban, and E. J. D. Vredenbregt, Ultracold electron sources, Int. J. Mod. Phys. A **22,** 3882 (2007).

[39] M. Reiser, *Theory and Design of Charged Particle Beams*, 2nd ed. (Wiley-VCH, New York, 2008).

[40] T. van Oudheusden, P. L. E. M. Pasmans, S. B. van der Geer, M. J. de Loos, M. J. van der Wiel, and O. J. Luiten, Compression of Subrelativistic Space-Charge-Dominated Electron Bunches for Single-Shot Femtosecond Electron Diffraction, Phys. Rev. Lett. **105**, 264801 (2010).

[41] T. van Oudheusden, Ph.D. thesis, Eindhoven University of Technology, 2010.

[42] P. L. E. M. Pasmans, Ph.D. thesis, Eindhoven University of Technology, 2014.

[43] F. B. Kiewiet, Ph.D. thesis, Eindhoven University of Technology, 2003.